Model-Based Prediction of the α-Hemolysin Structure in the Hexameric State

Simone Furini,*† Carmen Domene,† Michele Rossi,‡ Marco Tartagni,‡ and Silvio Cavalcanti*
*Department of Electronics, Computer Science and Systems, University of Bologna, Bologna, Italy; †Physical and Theoretical Chemistry Laboratory, Department of Chemistry, University of Oxford, Oxford, United Kingdom; and ‡ARCES: Advanced Research Center on Electronic Systems for Information and Communication Technologies "E. De Castro", University of Bologna, Bologna, Italy

ABSTRACT The α-hemolysin toxin self-assembles in lipid bilayers to form water-filled pores. In recent years, α-hemolysin has received great attention, mainly due to its possible usage as a sensing element. We measured the ion currents through single α-hemolysin channels and confirmed the presence of two different subpopulations of channels with conductance levels of 465 $\pm$ 30 pS and 280 $\pm$ 30 pS. Different oligomerization states could be responsible for these two conductances. In fact, a heptameric structure of the channel was revealed by x-ray crystallography, whereas atomic force microscopy revealed a hexameric structure. Due to the low resolution of atomic force microscopy the atomic details of the hexameric structure are still unknown, and are here predicted by computational methods. Several possible structures of the hexameric channel were defined, and were simulated by molecular dynamics. The conductances of these channel models were computed by a numerical method based on the Poisson-Nernst-Planck electrodiffusion theory, and the values were compared to experimental data. In this way, we identified a model of the α-hemolysin hexameric state with conductance characteristics consistent with the experimental data. Since the oligomerization state of the channel may affect its behavior as a molecular sensor, knowing the atomic structure of the hexameric state will be useful for biotechnological applications of α-hemolysin.

INTRODUCTION

α-Hemolysin (αH) is a pore-forming toxin secreted by the bacterium *Staphylococcus Aureus* and is a major determinant of bacterial pathogenicity (1). Despite wide knowledge about the functioning and structure of αH, the oligomerization state of the protein is still under debate. A heptameric structure was revealed by x-ray crystallography (2), whereas a hexameric structure was suggested by atomic force microscopy (AFM) data (3). Due to the low resolution of AFM, the atomic structure of the hexameric state is still unknown and is here predicted by numerical simulations.

Interest in the atomic structure of the hexameric state is justified by the technological relevance of the αH channel (4). Several characteristics make αH an ideal candidate for a sensing element in biotechnological applications. Hemolysins may bind directly to artificial or natural lipid membranes (5,6), and the binding does not require any auxiliary molecule or special experimental conditions. Once it is bound to the lipid bilayer, αH spontaneously oligomerizes to form a transmembrane channel (7), and the open state of the channel is stable and highly conductive (8). The possible use of αH as a sensing element has already been demonstrated in various fields, including 1), sensing of divalent metal ions (9); 2), sensing of organic molecules (10); 3), analysis of single-stranded RNA or DNA molecules (11); 4), detection of specific DNA or RNA sequences (12). The oligomerization state may affect the affinity of the channel for blocking molecules, and consequently its function as a molecular sensor. In this context, knowledge of the atomic structure of the different oligomerization states will prove useful.

The existence of two oligomerization states of the αH channels is also supported by electrophysiological measurements. To analyze the conduction characteristics of αH, it is important to distinguish between two phenomena: 1), the heterogeneous distribution of single-channel conductances in a population of channels; and 2), the changes of conductance within each subpopulation. The insertion of an αH channel in a lipid bilayer is experimentally revealed by a current step in the recording system. A heterogeneous distribution of the channel conductance refers to the fact that under fixed experimental conditions, the amplitudes of these current steps are distributed among different values. Histograms of single-channel currents have shown the presence of at least two current levels in a population of αH channels (8,13,14). Since no transitions were observed between conductance levels (13), it is possible to associate the different conductances with different subpopulations of αH channels (referred to here as high- and low-conductance states).

Experimental conditions influence the distribution of channels among the subpopulations (13), as well as the conductance characteristics within each subpopulation. Concerning the latter issue, a major role is played by divalent and trivalent cations, and by the pH of the bathing solutions. Divalent and trivalent cations inhibit conduction in αH channels by a blockage mechanism (8). On the other hand, pH modulates the channel conductance and the nonlinearity of the

Submitted December 4, 2007, and accepted for publication May 7, 2008.

Address reprint requests to Simone Furini, Dept. of Electronics, Computer Science and Systems, University of Bologna, Viale Risorgimento, 2. I-40136, Bologna, Italy. Tel.: 390512093067; Fax: 390512093540; E-mail: simone.furini@unibo.it.

Editor: Peter Tieleman.

0006-3495/08/09/2265/10 $2.00

doi: 10.1529/biophysj.107.127019

current-voltage relation (15). It has been shown that the influence of pH is primarily electrostatic (16): the protonation states of the protein molecule vary depending on the pH of the medium and, thus, the conduction characteristics of the channel. Together with these changes in conductance governed by the experimental conditions, an αH channel can also switch between an open and an almost-closed state through a mechanism that can be reversed by applying a zero membrane potential (17). The conductance of the ''closed'' state is ~10-fold lower than the conductance of the open state, despite the fact that the channel radius remains almost unchanged. This suggests that no severe structural changes of the channel take place during gating, and that instead changes in the protonation states of the amino acids facing the permeation pathway are likely to occur (18).

The changes in the channel current induced by the experimental conditions and by channel gating act on single αH channels, and should not be confused with the heterogeneous distribution of conductances in a population of channels. A possible explanation for the observation of different subpopulations of channels is that αH may exist in different structural forms that do not convert one to the other once the channel is embedded in the lipid bilayer. In agreement with Menestrina's ideas (8), we hypothesized that the subpopulations of αH channels are indeed channels with a different oligomerization state.

In the crystallographic structure of αH (2), seven identical monomers are symmetrically arranged around the channel axis (Fig. 1). The transmembrane domain of the channel has a β-barrel structure; each monomer contributes to the β-barrel by two antiparallel β-sheets. The β-barrel pore is connected to the extracellular compartment, by a wide protein domain (extracellular cap). This heptameric structure has been associated with the high-conductance state of the channel since the atomic structure was solved (2). Numerical simulations using different approaches (19–21) confirmed this hypothesis. Assuming that different oligomerization states are responsible for the two conductance values, and given the association between the heptameric structure and the high-conductance state, the low-conductance state with the hexameric structure remains to be identified.

To identify the atomic structure of the αH channel in the hexameric state, we took advantage of the experimental data on the heptameric state (2). It is assumed that the overall structure of the heptameric state is preserved in the hexameric state. The symmetrical structure revealed by AFM for the hexameric state supports this hypothesis (3). By analogy with the heptameric structure, the transmembrane pore of the hexameric channel would include 12 β-sheets, with each monomer contributing a couple of antiparallel sheets to the β-barrel. It is known that the hydrogen-bond network and the packing of the side chains restrict the admissible atomic structures in a β-barrel channel (22,23). According to these restrictions, we defined a set of atomic models for the transmembrane pore of the hexameric αH channel. The conductances of these hypothetical structures were computed using an approach based on the Poisson-Nernst-Planck theory, and were compared to experimental data to identify a proper model of the αH channel in the hexameric state.

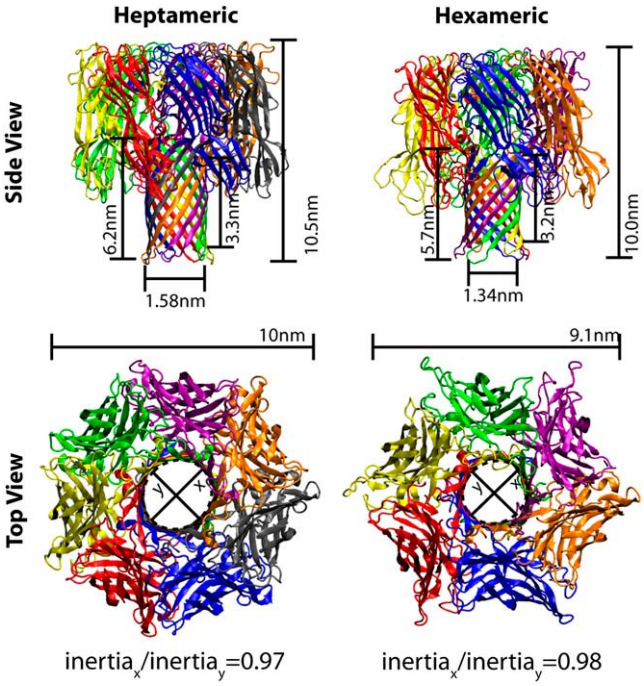

FIGURE 1 Heptameric structure and hexameric model of the αH channel. Side and top (extracellular) views of the αH channel in the heptameric (HEPTA-CAP model) and hexameric (HEXA-S16CAP model) states. Channel subunits are shown in cartoon representation, using different colors for each subunit. Vertical lines indicate the lengths of the β-barrel domain, the hydrophobic belt, and the entire channel. Horizontal lines in the side-view panels show the mean value of the internal diameter of the β-barrel domain as computed by the PNP equation solver (using the atomic radii from Nina et al. (30)). Horizontal lines in the top-view panels show the maximum external diameter of the extracellular cap. The ratio between the inertia momenta orthogonal to the channel axis is shown at the bottom of the figure. All the geometrical parameters are mean values during the MD simulations. The figure was generated with the molecular viewer software VMD (36).

METHODS

Heptameric channels

Two models of the heptameric αH channel were defined: in one, all the αH residues were included (HEPTA-CAP), and in the other, only the β-barrel domain, from residue Thr^{109} to residue Val^{149}, was considered (HEPTA-BARREL). Atomic coordinates were taken from the crystallographic structure of Song et al. (Protein Data Bank entry 7AHL) (2). Residues with missing atoms were built using the software *psfgen* of NAMD2 (24). Default protonation states were used for all the amino acids. Histidines were protonated at the delta position. N- and C-terminals were, respectively, acetylated and amidated. All crystallographic water molecules were included in the models.

The channel models were embedded in a preequilibrated lipid bilayer made up of 512 dimyristoylphosphatidylcholine (DMPC) molecules. The membrane was oriented in the *xy* plane, and the αH pore was oriented along the *z* axis. The hydrophobic belt of the αH β-barrel (amino acids Tyr^{118}–Gly^{126} and Ile^{132}–Ile^{142}) was centered in the lipid bilayer. DMPC molecules

<0.12 nm from protein atoms were removed together with crystallographic waters <0.2 nm from DMPC molecules. The system was solvated, and potassium and chloride ions were added to reach a 150 mM concentration, yielding a neutral system.

Hexameric channels

The β-sheet is one of the most common structural domains found in proteins. In proteins with a β-barrel structure, each β-sheet is bound by hydrogen bonds both to the previous and the next β-sheet in the sequence. The main geometrical features of a β-barrel are based on two parameters: the number of β-sheets (N) and the shear number (S). The shear number is defined as follows. Starting from residue k in the first β-sheet, move perpendicular to the strand around the barrel (H-bond direction) until the first β-sheet is crossed again. If l is the residue at the intersection, the shear number is $|l - k|$ (Fig. 2). Contiguous residues along a β-sheet have opposite orientation, whereas contiguous residues along the H-bond direction have the same orientation. As a consequence, S is an even number.

The relation between the number of β-sheets and the shear number defines the packing of the amino acids in the β-barrel. If $S > 2N$ or $S < N$, the tilt angle of the β-sheets causes a close packing of the side chains inside the channel. Actually, most of the β-barrel proteins satisfy the relation $N \le S \le 2N$ (22), and simple geometrical criteria identify $S = N + 4$ as the optimal relation, with twist and coil angles of the β-sheets closest to optimal values (23).

The heptameric structure of αH was used as a template to define a set of hexameric models. The transmembrane domain of the resulting hexameric models has a β-barrel structure with six pairs of antiparallel β-sheets, one pair from each subunit ($N = 12$). Four different starting structures were generated, with $S = 12$, 16, 20, and 24, placing the C^{α} atoms on a cylindrical surface with radius R, defined by

$$R = \frac{d_H}{2\sin\left(\frac{\pi}{N}\right)\cos(\alpha)} \qquad \alpha = \tan^{-1}\left(\frac{Sd_C}{Nd_H}\right), \qquad (1)$$

where d_H is the distance between consecutive β-sheets (0.44 nm); d_C is the C^{α}–C^{α} distance along the β-sheet (0.33 nm); and α is the β-sheet tilt angle with respect to the channel axis. C^{β} atoms were added to each C^{α} atom in the radial direction (C^{α}–C^{β} distance = 0.15 nm), with C^{β} atoms of consecutive residues facing alternately inward and outward. The remaining backbone heavy atoms were added to each residue on a plane tangent to the β-barrel surface. Residues Thr^{109}–Gly^{126} and Ile^{132}–Val^{149} of the heptameric crystal structure were moved, one by one, to residues in the hexameric model with the same side-chain orientation (inward or outward), using the C^{β} atom and the backbone atoms for the fitting. Subsequently, residues Asp^{127}–Lys^{131} of the heptameric structure were moved, using residues Gly^{126} and Ile^{132} for the fitting, to define the intracellular loops between β-sheets. Labels HEXA-S12, HEXA-S16, HEXA-S20, and HEXA-S24 will be used for the hexameric models with shear numbers 12, 16, 20, and 24, respectively.

Anticipating some of the results, the best agreement with the experimental data of the low-conductance state was given by the hexameric model with shear number 16 (see Results). Thus, the HEXA-S16 model of the transmembrane domain was chosen as the starting point for the entire αH channel in the hexameric state (transmembrane domain plus extracellular cap).

It was assumed that the structure of each monomer in the extracellular cap is preserved between the heptameric and the hexameric state, and that the monomers are symmetrically arranged around the channel axis. The atomic structure of each monomer was taken from the αH crystallographic structure (amino acids Ala^{1}–Thr^{109} and Val^{149}–Asn^{293}). Subsequently, the six monomers were symmetrically arranged around a central axis. Several structures were defined, characterized by different radial distances between monomers, thus by different radii of the extracellular cap. Each structure was superimposed on the HEXA-S16 model, using amino acids Thr^{109} and Val^{149} for the fitting procedure. The model of the extracellular cap closest to HEXA-S16 was selected (the distance between HEXA-S16 and the extracellular cap model was measured as the root mean-square deviation (RMSD) between amino acids Thr^{109} and Val^{149}). Residues Ala^{1}–Asp^{108} and Gln^{150}–Asn^{293} of this model of the extracellular cap, together with residues Thr^{109}–Val^{149} of HEXA-S16, defined the model of the entire αH channel in the hexameric state (HEXA-S16CAP).

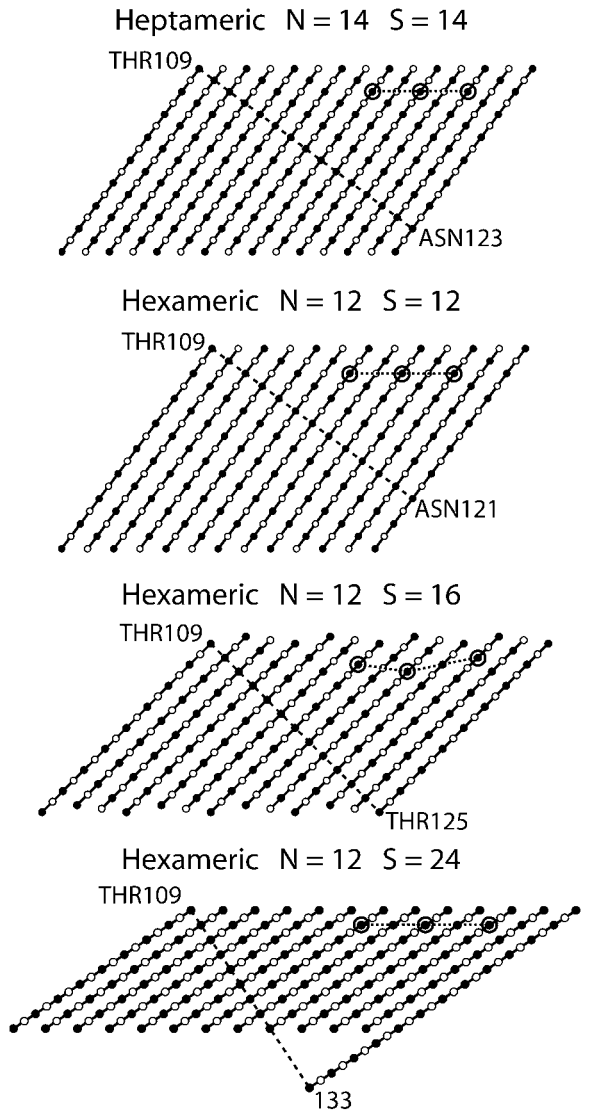

FIGURE 2 Unrolled β-barrel structures. β-sheet arrangements in β-barrels are schematically shown by unrolling the β-barrel surface on a plane. Continuous lines show the β-sheet directions, with open circles for amino acids pointing outward, and solid circles for amino acids pointing toward the pore lumen. Dashed lines run orthogonal to the β-sheets on the β-barrel surface (H-bond direction) and are used to define the shear numbers (S). Dotted lines with circles are used to highlight the relative position of analogous amino acids (in this case, Glu^{111}) on adjacent subunits. These amino acids are aligned along the channel axis if $S = N$ or $S = 2N$, but are no longer aligned if $S = N + 4$.

The hexameric models were embedded in a DMPC lipid bilayer and solvated, using the same procedure described previously for the heptameric models.

Molecular dynamics

The following protocol was employed for the molecular dynamics simulation of each model. Energy was first minimized by a steepest-descent procedure

(10,000 steps), followed by an equilibration period (500 ps) where harmonic potentials were applied to the backbone atoms of the protein (force constant set to 4 Mcal mol^{-1} nm^{-2}). Harmonic restraints on protein atoms were then removed, and unrestrained molecular dynamics (MD) simulation was run for 4 ns in the NPT ensemble.

The MD simulations were performed using the NAMD2 software (24), the CHARMM27 force field for protein and lipids (25), and the TIP3 model for water molecules (26). Periodic boundary conditions were adopted, and the long-range electrostatic interactions were treated by the particle mesh Ewald algorithm (27). A 1.2-nm smoothed cutoff was used for the van der Waals interactions. Hydrogen-bond lengths were fixed by the SHAKE algorithm (28), to use a 2-fs time step. The temperature was controlled by the Langevin algorithm at 300 K, with a damping coefficient of 5 ps^{-1}. Pressure was kept at 1 atm by the Nose-Hoover Langevin piston pressure control (29), with a piston period of 200 fs, and a damping time constant of 100 fs.

Poisson-Nernst-Planck theory

Poisson-Nernst-Planck (PNP) theory describes the steady-state fluxes of M ion species by the Poisson and Nernst-Planck equations:

$$\nabla \cdot (\varepsilon \nabla \phi) = -\rho - \sum_{i=1}^{M} z_i e C_i \tag{2}$$

$$\nabla \cdot J_i = 0 \qquad i = 1, \ldots, M$$
$$J_i = -D_i \left(\nabla C_i + z_i \frac{e}{kT} C_i \nabla \phi \right), \tag{3}$$

where ϕ is the electric potential; C_i, D_i, J_i, and z_i are the concentration, diffusion coefficient, flux, and valence, respectively, of the ith ion specie; ρ is the density of fixed electric charge; and ε is the dielectric constant (e, k, and T, are the elementary charge, the Boltzmann constant, and the temperature, respectively). In the Poisson equation (Eq. 2) ρ is the protein charge, which is fixed in space in contrast to ionic charges. Only the protein-charge distribution was explicitly modeled, whereas the lipid bilayer was assumed to be electrically neutral. Two monovalent ion species were included in the mathematical model, to simulate potassium and chloride ions.

PNP equations were solved on a cylindrical grid, with the z axis along the channel axis. The grid length was 13 nm in the axial direction, and 6 nm in the radial direction. The number of grid points was 130 in the axial direction, 120 in the radial direction, and 72 in the angular direction. Partial atomic charges were from the CHARMM27 force field (25). Atomic radii were defined according to the value proposed by Nina et al. (30). The relative dielectric constant was set to 2 for the protein and 80 for the water solution. A waterproof slice was placed around the channel, orthogonal to the pore. This slice was introduced to mimic the lipid bilayer; its relative dielectric constant was set to 2 and its width to 2.9 nm. The center of the slice was set to the center of the hydrophobic belt of αH (Tyr^{118}–Gly^{126} and Ile^{132}–Ile^{142}). Outside the channel, the diffusion coefficients were set to the experimental values for diffusion in free solution ($D_{K+} = 1.96 \times 10^{-9}$ m^2/s and $D_{Cl-} = 2.03 \times 10^{-9}$ m^2/s (31)). Diffusion coefficients were reduced inside the channel to take into account the confinement effects due to the pore finite size. The analytical expression proposed by Noskov et al. (20) was used to define the diffusion coefficients on each slice of the cylindrical grid inside the channel:

$$D = \frac{D_{bulk}}{6.43 \times 10^{-1} + 4.40 \times 10^{-4} e^{\frac{R_{ion}}{0.069 R_{pore}}} + 3.56 \times 10^{-1} e^{\frac{R_{ion}}{0.19 R_{pore}}}},$$

where R_{pore} is the radius of the pore; R_{ion} is the radius of the diffusing ion; and D_{bulk} is the diffusion coefficient in free solution; and numerical values were obtained fitting the diffusion coefficients of spherical particles in cylindrical pores (32).

PNP equations were solved by an iterative algorithm previously used to model potassium channels (33,34), with a tolerance of 10^{-10} mV for the Poisson equation, and 10^{-10} mM for the Nernst-Planck equations. To take into account the movements of the protein, PNP calculations were repeated on several snapshots of the MD trajectories. Structures were selected from the last 3 ns of the MD trajectories every 0.5 ns.

Experimental measurements

The planar lipid bilayer workstation from Warner Instrument (Harvard Apparatus, Holliston, MA) was used for single-channel recording. The bilayer apparatus consists of two chambers (1 ml each), connected by a 150-μm orifice through a Delrin cap. Lipid bilayers of α-phosphatidylcholine were formed by the painting method, using a diluted phosphatidylcholine solution in decane (15 mg/ml). Ag/AgCl electrodes connected the bathing solutions to the recording systems. The electrode in the *cis* chamber—where αH was added—was connected to the virtual ground. A positive potential indicates a higher potential in the *trans* chamber, and positive currents flow from *trans* (intracellular side of the channel) to *cis* (extracellular side of the channel). The membrane potential was clamped at +40 mV, and the insertion of a channel in the lipid bilayer was revealed by a current step in the recording system. The current-voltage relation was acquired by varying the membrane potential from −100 mV to 100 mV, with a 20-mV step. The protocol used to measure the current-voltage relation was repeated several times (>10) for each channel, to test the stability of the conductance. The timescale of the entire experimental protocol was ~5 min. Bathing solutions contained 0.5 M KCl, 10 mM EGTA, 10 mM HEPES (pH 7.5 with KOH). Signals were recorded with an Axopatch 200B amplifier, and data were analyzed by pCLAMP9 (Axon Instruments, Union City, CA). Signals were sampled at 10 kHz and filtered at 5 kHz. Experiments were conducted at a room temperature of 20 ± 2°C. All reagents were from Sigma (Milan, Italy).

RESULTS

Molecular dynamics simulations

Both heptameric models (HEPTA-CAP and HEPTA-BARREL) proved to be stable during MD trajectories (Fig. 3). Removing the extracellular cap did not affect the structural stability of the β-barrel domain. The higher RMSD of the backbone atoms in the HEPTA-BARREL model can be attributed to atomic displacements at the extracellular side as a consequence of the lack of extracellular cap.

The moment of inertia tensor of the β-barrel domain was used to evaluate the geometrical features of the pore, namely

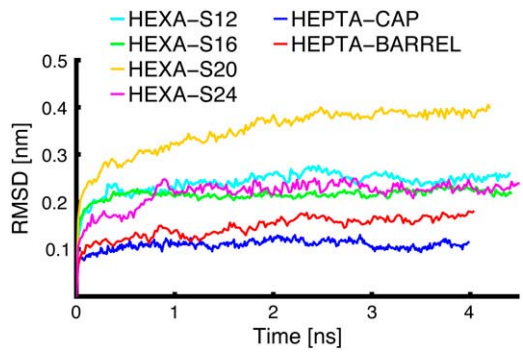

FIGURE 3 Root mean-square deviation of β-barrel domain. Root mean-square deviation was computed on the backbone atoms of residues Thr^{109}–Val^{149} for the various simulations.

the tilting of the pore with respect to the lipid membrane and the eccentricity of the β-barrel cross section. As a consequence of the cylindrical structure of the β-barrel, a principal axis of inertia is directed along the pore axis. The angle between this principal axis and the z axis measures the tilting of the channel in the lipid membrane. The maximum tilt was $<5°$ in both of the heptameric models. To estimate the cross section eccentricity, the inertia momenta along the principal axes orthogonal to the pore were used. The ratio between the minor and the major of these two inertia momenta is 1 in a β-barrel with circular cross section, whereas it decreases in a β-barrel with elliptical cross section. The mean ratio was 0.97 in both heptameric models, which suggests an almost circular cross section. A cross section more asymmetrical, but again close to circular, was observed by Aksimentiev and Schulten in a 50-ns MD simulation of αH (19) (ratio between inertia momenta $\approx$ 0.9). This deviation could be explained by differences in the length of the simulations and in the method employed to estimate the cross section asymmetry.

The number of hydrogen bonds in the β-barrel backbone was compared in the two heptameric models. Donor and acceptor atoms were counted as involved in a hydrogen bond when their distance was <0.4 nm and the donor-hydrogen-acceptor angle was between 160° and 200° (35). The mean numbers of hydrogen bonds were 180 and 172 in the HEPTA-CAP and HEPTA-BARREL models, respectively. The greater mobility of the extracellular side causes the decrease of hydrogen bonds in the HEPTA-BARREL model.

The four hexameric models of the transmembrane domain (HEXA-S12, HEXA-S16, HEXA-S20, and HEXA-S24) were stable during the MD simulations (Fig. 3). The pore axis was orthogonal to the lipid membrane in channel models HEXA-S12 and HEXA-S16, with maximum deviations of $<3°$. A higher deviation was observed in both the HEXA-S20 ($\sim$14°) and HEXA-S24 models ($\sim$10°). The cross section was almost circular in the HEXA-S12 and HEXA-S16 models (ratio between the inertia momenta = 0.98 in both models). The cross section asymmetry was more pronounced in the HEXA-S20 and HEXA-S24 models (ratio = 0.88 and 0.85, respectively). The mean number of hydrogen bonds was 120 in HEXA-S20 and close to 140 in HEXA-S12, HEXA-S16, and HEXA-S24. This number of hydrogen bonds corresponds to 57% of oxygen backbone atoms involved in hydrogen bonds, the same percentage as in the HEPTA-BARREL model.

The HEXA-S16CAP model (with extracellular cap) exhibited structural characteristics of the β-barrel domain analogous to the structural characteristics revealed in the HEXA-S16 model (no extracellular cap). In the MD simulation of HEXA-S16CAP, the channel axis stayed orthogonal to the lipid membrane (maximum deviation $<3°$); the cross section of the pore was close to circular (ratio between inertia momenta = 0.98); and the mean number of hydrogen bonds in the β-barrel domain was $\sim$140. The length of the HEXA-S16CAP model along the channel axis was 10 nm, and the external diameter of the extracellular cap was 9.1 nm. The analogous values measured by AFM were 9.7 $\pm$ 1.2 nm and 7.6 $\pm$ 0.4 nm (3). The extracellular cap was stable during the MD trajectory, with an RMSD of the backbone atoms <0.2 nm. Changing the oligomerization state from heptameric to hexameric influenced the packing of the monomers and, hence, the contact area between adjacent subunits. The buried surface area between two adjacent subunits was $\sim$58.97 nm^2 in the HEPTA-CAP model, and $\sim$50.55 nm^2 in the HEXA-S16CAP model, with a reduction close to 20% (buried surface area was computed by the VMD software (36), using a probe radius of 0.14 nm). The decrease in the buried surface area between adjacent subunits was somehow expected, due to the transition from heptameric to hexameric symmetry. Nevertheless, most of the intersubunit interactions observed in the crystallographic structure (2) were preserved in the simulation of the HEXA-S16CAP model. The salt bridges between Lys^{58} and Asp^{100}, Lys^{147} and Glu^{111}, and Lys^{110} and Asp^{152} were stable during the MD simulation (mean length <0.35 nm); and $\sim$75 hydrogen bonds connected adjacent subunits of the HEXA-S16CAP model. These include the hydrogen bonds at the N-terminal latch (residues Ala^1–Val^{20}), which are important (37), even if not essential (38), for an efficient oligomerization of the αH channel. As a final remark about the structure of the extracellular cap in the HEXA-S16CAP model, water channels appeared between adjacent subunits in the 4-ns MD simulation. These side channels connect the interior of the αH pore to the extracellular solution and to the rim region (lower boundary of the extracellular cap). Similar water channels were also observed in MD simulations of the HEPTA-CAP model and of the heptameric αH channel by Aksimentiv and Schulten (19).

Channel conductances

Experimental measurements in 0.5 M KCl revealed two different current-voltage relations for the αH channels (Fig. 4). Data were associated with the high- or low-conductance state according to the conductance at 40 mV, using a value of 400 pS as the threshold level. Once a channel was assigned to the high- or low-conductance state, no transitions to the other state were observed. The high and low conductances at 40 mV were 465 $\pm$ 30 pS and 280 $\pm$ 30 pS (Fig. 4). The experimental current-voltage relations of αH were slightly asymmetric, with higher conductance at positive membrane potential. The ratio between the channel conductances at +40 mV and −40 mV was 1.2 for both the high- and low-conductance states.

The PNP theory provided a channel conductance of 680 $\pm$ 25 pS for the HEPTA-CAP model at 40 mV. The mean values and the standard deviations of the channel currents were computed by repeating the PNP calculations on different snapshots from the MD simulation. The predicted conductance overestimated the experimental high-conductance value by 1.5-fold (Fig. 4).

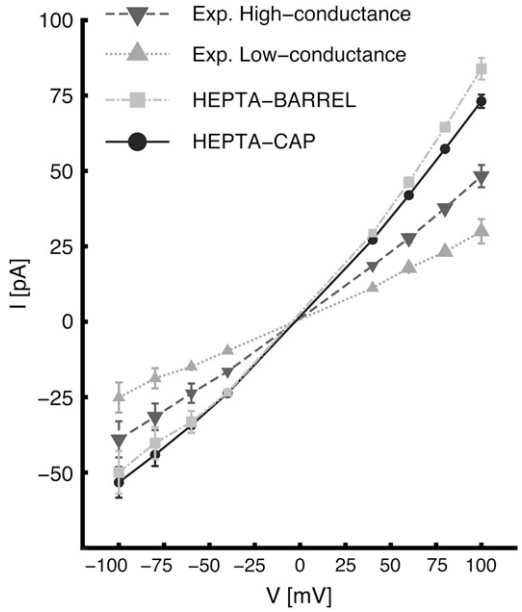

FIGURE 4 Current-voltage relations in the experimental data and heptameric models. Experimental currents for the high-conductance state (▼, *dashed line*), the low-conductance state (▲, *dotted line*), the computed currents in the HEPTA-CAP model (●, *solid line*), and the computed currents in the HEPTA-BARREL model (■, *dash-dotted line*). Mean values and standard deviations of the experimental currents were defined using 10 independent measurements, whereas six different snapshots of the MD simulations were used for the computed currents. Standard deviations are shown as vertical lines when larger than the markers used for the mean values. Potassium and chloride concentrations in the intracellular and extracellular compartments were 0.5 M for both the experimental and theoretical data.

The asymmetry in the current-voltage relation was well reproduced by the PNP approach. The ratio between the computed channel conductances at +40 mV and −40 mV was 1.2 ± 0.1, in agreement with the experimental data. The HEPTA-CAP model was slightly selective to anions, having a ratio between cationic and anionic flux equal to 0.77 ± 0.18. To better estimate the selectivity, channel currents were computed in the presence of concentration gradients, and the reversal potentials were then estimated. The reversal potential is related to channel selectivity by the Goldman-Hodgkin-Katz equation:

$$V_{\text{rev}} = \frac{kT}{e} \ln\left[\frac{P_{\text{K}}[C]_{\text{e}} + P_{\text{Cl}}[C]_{\text{i}}}{P_{\text{K}}[C]_{\text{i}} + P_{\text{Cl}}[C]_{\text{e}}}\right],$$

where P_{K} and P_{Cl} represent the permeability to potassium and chloride ions, respectively, and $[C]_{\text{e}}$ and $[C]_{\text{i}}$ are the ionic concentrations in the extracellular and intracellular compartments, respectively. The reversal potentials were −3.4 mV with $[C]_{\text{e}} = 1$ M and $[C]_{\text{i}} = 0.2$ M ($P_{\text{K}}/P_{\text{Cl}} = 0.8$) and +5.6 mV with $[C]_{\text{e}} = 2$ M and $[C]_{\text{i}} = 1$ M ($P_{\text{K}}/P_{\text{Cl}} = 0.7$). Under the same conditions, Gu et al. (39) experimentally measured reversal potentials of −3.7 mV and +9.1 mV, respectively.

The analysis of the HEPTA-BARREL model provided similar results (Fig. 4). The HEPTA-BARREL conductance was 730 ± 30 pS at +40 mV; the ratio between the channel conductances at +40 mV and −40 mV was 1.3 ± 0.1, and the ratio between cationic and anionic fluxes was 0.79 ± 0.10. Considering that removing the extracellular domain did not affect the computed currents remarkably, the theoretical conductances of the hexameric models lacking the extracellular cap were compared to the experimental data of the low-conductance state.

Ionic currents through HEXA-S20 and HEXA-S24 overestimated the experimental data by three- and sevenfold, respectively, whereas the HEXA-S12 model underestimated the experimental data (Fig. 5). The HEXA-S16 model showed the best agreement with the experimental low-conductance value. The predicted conductance at 40 mV was 370 ± 25 pS, which overestimates the low-conductance experimental value by 1.3-fold.

The current-voltage relation of the HEXA-S16 model was slightly asymmetric (ratio between the computed channel conductances at +40 mV and −40 mV equal to 1.1 ± 0.1), in agreement with the experimental results. The anionic selectivity was somewhat higher than in the heptameric models (ratio between cationic and anionic fluxes equal to 0.63 ± 0.14). The reversal potentials were −9.1 mV with $[C]_{\text{e}} = 1$ M and $[C]_{\text{i}} = 0.2$ M ($P_{\text{K}}/P_{\text{Cl}} = 0.6$) and +7.9 mV with $[C]_{\text{e}} = 0.2$ M and $[C]_{\text{i}} = 1$ M ($P_{\text{K}}/P_{\text{Cl}} = 0.6$). The tighter packing of

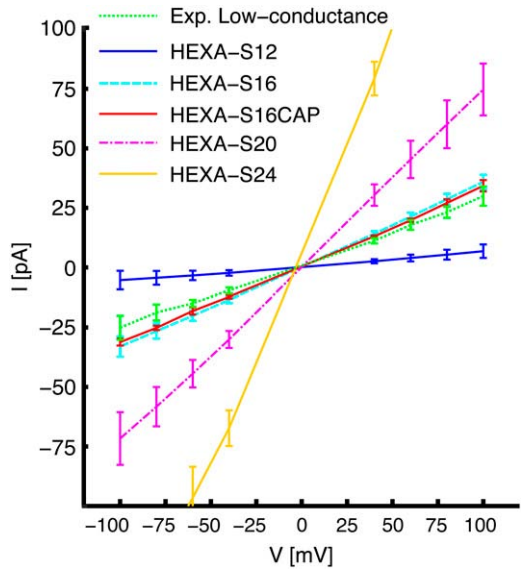

FIGURE 5 Current-voltage relations in the low-conductance state. Experimental currents for the low-conductance state (*dotted green line*), and the computed currents in the HEXA-S12 model (*solid blue line*), HEXA-S16 model (*dashed cyan line*), HEXA-S20 model (*dot-dashed purple line*), HEXA-S24 model (*solid yellow line*), and HEXA-S16CAP model (*solid red line*). Mean values and standard deviations of the experimental currents were defined using 10 independent measurements, whereas six different snapshots of the MD simulations were used for the computed currents. Potassium and chloride concentrations in the intracellular and extracellular compartments were 0.5 M for both the experimental and theoretical data.

the charged residues in the HEXA-S16 model, compared to the heptameric models, justifies the higher anionic selectivity.

Since the HEXA-S16 model showed the best agreement with the experimental data of the low-conductance state, the conductance calculations were repeated in the HEXA-S16CAP model. As observed for the models of the heptameric channel, the hexameric model with the extracellular cap has a lower conductance than the model without the extracellular cap. The conductance of the HEXA-S16CAP model at +40 mV was 335 ± 10 pS, compared to 370 ± 25 pS in the HEXA-S16 model. This conductance overestimates the experimental value of the low-conductance state by ~1.2-fold. The current-voltage relation was slightly asymmetric (ratio of 1.1 ± 0.1 between the conductances at +40 mV and −40 mV), and the channel was anion-selective. The ratio between cationic and anionic fluxes was 0.36 ± 0.13, lower than the value computed in the HEXA-S16 model (0.63 ± 0.14). The tighter packing of positively charged residues, such as Lys[8], in the hexameric structure might cause the increased selectivity observed in the HEXA-S16CAP model. The internal radius of the extracellular cap is smaller in the hexameric structure compared to the heptameric structure (0.97 nm vs. 1.30 nm). Therefore, the effect of the protein charges on the permeating ions is more substantial, which explains why absence of the extracellular cap affects the selectivity of the hexameric models and not that of the heptameric models.

The electrostatic potential and the ion distributions inside the channel were computed by the PNP theory to compare the channel models HEPTA-CAP, HEPTA-BARREL, HEXA-S16CAP, and HEXA-S16 (Fig. 6). The remarkable similarity in electrostatic potential and ion distributions between the heptameric models supports the hypothesis that the β-barrel domain is the major determinant of the conduction characteristics, whereas the extracellular cap plays a minor role. The similarity is also evident between the HEXA-S16CAP and HEXA-S16 models. However, a peak in chloride concentration is observed at the extracellular side of the HEXA-S16CAP model, close to the ring of positively charged amino acids Lys[8]. The presence of this peak is consistent with the increase in anionic selectivity induced by the introduction of the extracellular cap in the model of the hexameric channel. The hexameric models differ from the heptameric models in the electrostatic potential and ion distributions inside the channel (Fig. 6). The chloride concentration is higher in the hexameric models at both the extracellular and intracellular entrances of the β-barrel, and the potassium depletion from these regions is stronger. These characteristics correlate with the higher anionic selectivity of the hexameric models.

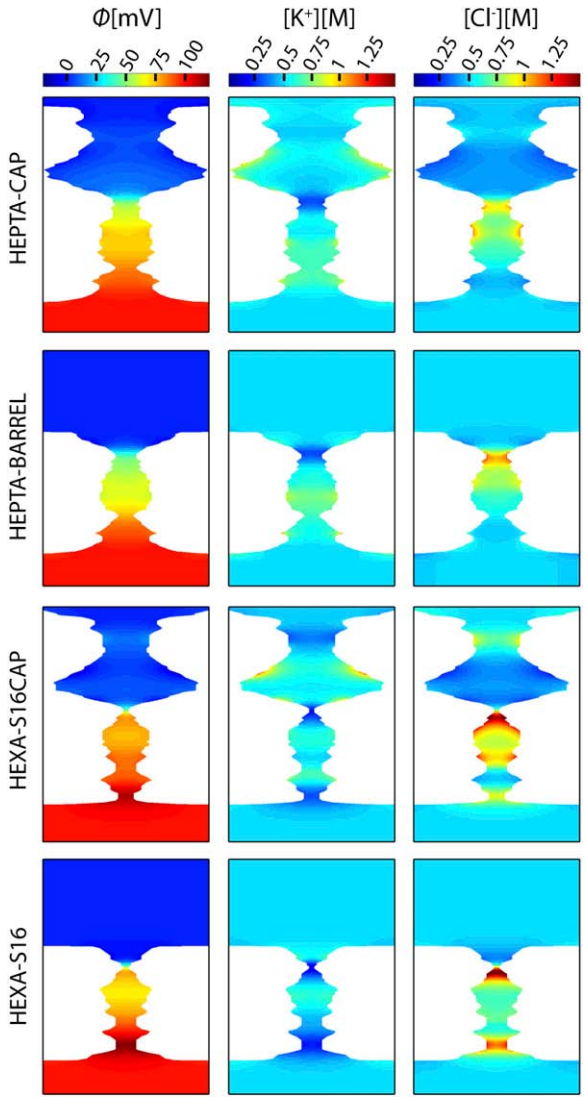

FIGURE 6 Electrostatic potential and ion concentrations. Electrostatic potential and ion concentrations of a longitudinal section of the channel models are shown. Membrane potential was set to +100 mV and extracellular and intracellular ion concentrations to 500 mM. The same color ranges defined by the horizontal bars on the top of the figure are used for the electrostatic potential and ion concentrations in all the channel models.

DISCUSSION

The αH channel may exist in different oligomerization states, namely, heptameric and hexameric. Although the atomic structure of the heptameric state was solved by x-ray crystallography (2), the hexameric structure is known only at low resolution from AFM experiments (3). Considering the β-barrel nature of the transmembrane domain of αH, several potential atomic structures of the hexameric channel were defined, using geometric rules (22,23). The conduction characteristics of these hypothetic structures were determined by computational methods, and compared to experimental data. Values for experimental conductance were reproduced by the hexameric model with a shear number of 16, which we propose as the most likely atomic structural model of the αH channel in the hexameric state.

The experimental conductance of the αH channel has been estimated by Aksimentiev and Schulten using MD simula-

tions, with a description of the atomistic details of the conduction process (19). Here, to compute the channel conductance, a simplified approach based on the PNP theory was preferred over more complex and computationally expensive MD simulations. Employing a computational method based on the PNP equations significantly decreases the computational load, allowing a realistic comparison between different channel models at different boundary conditions, like the one presented here.

Electrodiffusion theory has been widely used to model ion channels, and has proved to reproduce accurately a large amount of experimental data (40,41). Nevertheless, the PNP approach suffers from two main shortcomings: 1), ions are described by a continuum distribution, ignoring their discrete nature; and 2), the atomic motions of the channel protein are neglected. To evaluate the role of atomic motion in channel conductance, PNP calculations were performed on several snapshots from the MD trajectories. The methodology was first tested in the heptameric αH channel. In both heptameric models, with and without the extracellular cap, the PNP approach overestimated the experimental high-conductance value by $\sim$1.5-fold. It is important to remember that: 1), no parameter was employed to fit the experimental data; and 2), the asymmetry of the current-voltage relation and the channel selectivity were well reproduced.

The purpose of this study was to model a plausible atomic structure for the αH channel in the hexameric state, not to validate the PNP approach. The parameters of the PNP mathematical model can always be adjusted to better reproduce the experimental currents, as shown in a recent work by O'Keeffe et al. (42), where perfect agreement with the experimental data was obtained by increasing the relative dielectric constant of the channel to $\sim$20. In the context of the study presented here, where we are trying to identify a model for the hexameric structure of the αH channel, this issue is partially irrelevant. The error introduced by the PNP theory is influenced by the strength of the ionic solution: the overestimation of the channel conductance is higher at higher ionic concentrations, and the nonlinearity of the current-voltage relation is overestimated at low ionic concentrations (20). A KCl concentration of 0.5 M was chosen to yield a good estimate of both the channel conductance and the current-voltage relation asymmetry. Since we are comparing similar structures (the heptameric and the hexameric αH channels) at the same ionic concentrations, the error introduced by the PNP theory is assumed to be systematic, i.e., once the overestimation in the current is known for the heptameric model, a similar value ($\sim$1.5) is expected in the hexameric model.

The low sensitivity of the PNP results to the MD snapshot, and the agreement with the experimental data on channel selectivity and current-voltage relation, suggest that the PNP approach provides a reliable description of conduction in the αH channel, and that this approach can be used to analyze the hexameric models. In the first phase, the analysis of the hexameric models focused on the β-barrel domain; this is the domain governing the conduction characteristics of the αH channel, as proved by experimental data (39,43), previous computational works (16,20), and our results on the HEPTA-CAP and the HEPTA-BARREL models. The β-barrel architecture of the transmembrane domain guided the definition of the hexameric models for this region of the channel. In contrast, defining a model for the extracellular cap is more ambiguous, since the structure of this domain is not as regular as the structure of the β-barrel domain, and only AFM images are available. Focusing the analysis on the transmembrane domain allowed the identification of a plausible structure for this relevant region of the protein and excluded any artifact due to the speculative nature of the extracellular cap model.

All the hexameric models of the transmembrane domain were stable during the simulation time, although the temporal scale of the MD simulations does not allow a comparison of the energetic stability of the different channel structures. Instead, the calculation of the values of the channel conductance allowed a selection among the hexameric models. The hexameric model with shear number 16 was the one in better agreement with the experimental data. Noteworthy is the fact that the overestimation of the low-conductance value by the HEXA-S16 model is similar to the overestimation of the high-conductance value by the heptameric channel models, which strengthens the identification of the HEXA-S16 model as the plausible structure of the transmembrane domain of the αH channel in the hexameric state.

Once a structure for the transmembrane domain of hexameric αH was selected, the transmembrane model was completed with the extracellular cap. To define the extracellular cap, it was assumed that the structure of each monomer and the cylindrical symmetry were conserved between the heptameric and hexameric channels. These assumptions are consistent with the experimental data reported by AFM, but nevertheless, different structures are possible. It is worth mentioning that the intersubunit interactions important for oligomerization of the heptameric channel are conserved in the hexameric model.

A different structure of the hexameric αH channel, with a shear number of 12, was proposed by Smart et al. (44), according to experimental data by Korchev et al. (17). In the Korchev et al. study (17), a 1:10 ratio between the low- and the high-conductance values was suggested. In our experimental data, the ratio was 1:1.5, in agreement with previous results by Belmonte et al. (13). The high and low values of conductance obtained in our measurements referred to different channels. Once a channel entered in the lipid membrane, it showed a specific conductance (high or low), and no transitions to a different value were observed. This behavior is consistent with the idea that the channel may enter the membrane in different oligomerization states, characterized by different values of conductance. In contrast, the states described by Korchev et al. (17) correspond to open and closed conformations of the same channel, and consequently it is unlikely that they are related to different oligomerization

states of αH. A change in the oligomerization state requires breaking and forming of a high number of hydrogen bonds, which is unlikely to occur once the channel is inserted in the lipid membrane.

The PNP approach made it possible to analyze the current-voltage relation and the selectivity of the hexameric channels. As expected, these were very similar to the analogous properties of the heptameric channels. However, an increased anionic selectivity was observed in the hexameric model, which suggests that the hexameric and heptameric channels might demonstrate different behavior. In fact, in the models proposed, not only does the hexameric channel have an internal radius lower than that of the heptameric channel, but it also shows different spatial alignment of the amino acids in adjacent subunits. Analogous amino acids in adjacent subunits are aligned along the channel axis in β-barrel structures with $S = N$ (heptameric structure), but they are no longer aligned in structures with $S = N + 4$ (hexameric structure; see Fig. 2). These differences in the internal profile and in the relative positions of adjacent subunits may affect the interactions of the channel with permeating molecules, like molecular adapters.

Molecular adapters have been used to functionalize αH channels for technological applications (10,45–47). For instance β-cyclodextrin binds along the permeation pathway of αH, creating a constriction with specific selectivity for various organic molecules (10). β-Cyclodextrin has a heptameric structure, which makes this cyclic oligosaccharide the optimal choice for binding to a heptameric channel. A closely related cyclic oligosaccharide—α-cyclodextrin—has instead a hexameric structure, and thus a hexameric channel is expected to have a higher affinity to α-cyclodextrin than to β-cyclodextrin. To the best of our knowledge, analysis of the β-cyclodextrin binding in αH is restricted to channels in high-conductance states. Our data show that the low-conductance state of αH can be supported by the presence of channels with hexameric structure. Analyses of the binding affinity of cyclodextrins to αH channels in the low-conductance state could be used to test this hypothesis.

A problem connected to the usage of molecular adapters like cyclodextrins in technological applications is the unstable binding mode between the channel and the adapter. The residence time of β-cyclodextrin inside the αH channel is restricted to hundreds of microseconds, and although it can be extended by three orders of magnitude through amino acid mutations along the permeation pathway (43), unstable binding is indeed a limitation for the development of stochastic sensors. If the channel model proposed here actually represents the low-conductance state of αH, the binding characteristics of a molecular adapter in the high- and low-conductance states should be different, and these differences may help in improving the characteristics of biosensors based on αH channels.

The authors gratefully acknowledge Francesco Lodesani for helpful discussions, and CINECA (Bologna, Italy) for providing supercomputing time. C.D. thanks The Royal Society for a University Research Fellowship and the Engineering and Physical Sciences Research Council's National Service for Computational Chemistry Software.

REFERENCES

1. Bhakdi, S., and J. Tranum-Jensen. 1991. α-toxin of *Staphylococcus aureus*. *Microbiol. Rev.* 55:733–751.
2. Song, L., M. R. Hobaugh, C. Shustak, S. Cheley, H. Bayley, and J. E. Gouaux. 1996. Structure of staphylococcal α-hemolysin, a heptameric transmembrane pore. *Science*. 274:1859–1866.
3. Czajkowsky, D. M., S. Sheng, and Z. Shao. 1998. Staphylococcal α-hemolysin can form hexamers in phospholipid bilayers. *J. Mol. Biol.* 276:325–330.
4. Kang, X. F., S. Cheley, A. C. Rice-Ficht, and H. Bayley. 2007. A storable encapsulated bilayer chip containing a single protein nanopore. *J. Am. Chem. Soc.* 129:4701–4705.
5. Freer, J. H., J. P. Arbuthnott, and A. W. Bernheimer. 1968. Interaction of staphylococcal α-toxin with artificial and natural membranes. *J. Bacteriol.* 95:1153–1168.
6. Ferreras, M., F. Hoper, M. D. Serra, D. A. Colin, G. Prevost, and G. Menestrina. 1998. The interaction of *Staphylococcus aureus* bi-component γ-hemolysins and leucocidins with cells and lipid membranes. *Biochim. Biophys. Acta.* 1414:108–126.
7. Valeva, A., M. Palmer, and S. Bhakdi. 1997. Staphylococcal α-toxin: formation of the heptameric pore is partially cooperative and proceeds through multiple intermediate stages. *Biochemistry.* 36:13298–13304.
8. Menestrina, G. 1986. Ionic channel formed by *Staphylococcus aureus* α-toxin: voltage dependent inhibition by divalent and trivalent cations. *J. Membr. Biol.* 90:177–190.
9. Braha, O., L.-Q. Gu, L. Zhou, X. Lu, S. Cheley, and H. Bayley. 2000. Simultaneous stochastic sensing of divalent metal ions. *Nat. Biotechnol.* 18:1005–1007.
10. Gu, L.-Q., O. Braha, S. Conlan, S. Cheley, and H. Bayley. 1999. Stochastic sensing of organic analytes by a pore-forming protein containing a molecular adapter. *Nature.* 398:686–690.
11. Kasianowicz, J. J., E. Brandin, D. Branton, and D. W. Deamer. 1996. Characterization of individual polynucleotide molecules using a membrane channel. *Proc. Natl. Acad. Sci. USA.* 93:13770–13773.
12. Howorka, S., S. Cheley, and H. Bayley. 2001. Sequence-specific detection of individual DNA strands using engineered nanopores. *Nat. Biotechnol.* 19:636–639.
13. Belmonte, G., L. Cescatti, B. Ferrari, T. Nicolussi, M. Ropele, and G. Menestrina. 1987. Pore formation by *Staphylococcus aureus* α-toxin in lipid bilayers. Dependence upon temperature and toxin concentration. *Eur. Biophys. J.* 14:349–358.
14. Krasilnikov, O. V., P. G. Merzlyak, L. N. Yuldasheva, C. G. Rodrigues, S. Bhakdi, and A. Valeva. 2000. Electrophysiological evidence for heptameric stoichiometry of ion channels formed by *Staphylococcus aureus* α-toxin in planar lipid bilayers. *Mol. Microbiol.* 37:1372–1378.
15. Kasianowicz, J. J., and S. M. Bezrukov. 1995. Protonation dynamics of the α-toxin ion channel from spectral analysis of pH-dependent current fluctuations. *Biophys. J.* 69:94–105.
16. Misakian, M., and J. J. Kasianowicz. 2003. Electrostatic influence on ion transport through the aHL channel. *J. Membr. Biol.* 195:137–146.
17. Korchev, Y. E., C. L. Bashford, G. M. Alder, J. J. Kasianowicz, and C. A. Pasternak. 1995. Low conductance states of a single ion channel are not ''closed''. *J. Membr. Biol.* 147:233–239.
18. Korchev, Y. E., C. L. Bashford, G. M. Alder, P. Y. Apel, D. T. Edmonds, A. A. Lev, K. Nandi, A. V. Zima, and C. A. Pasternak. 1997. A novel explanation for fluctuations of ion current through narrow pores. *FASEB J.* 11:600–608.
19. Aksimentiev, A., and K. Schulten. 2005. Imaging α-hemolysin with molecular dynamics: ionic conductance, osmotic permeability, and the electrostatic potential map. *Biophys. J.* 88:3745–3761.

20. Noskov, S. Y., W. Im, and B. Roux. 2004. Ion permeation through the α-hemolysin channel: theoretical studies based on Brownian dynamics and Poisson-Nernst-Plank electrodiffusion theory. *Biophys. J.* 87:2299–2309.

21. Cozmuta, I., J. T. O'Keeffe, B. Deepak, and V. Stolc. 2005. Hybrid MD-Nernst-Planck model of the α-hemolysin conductance proprieties. *Mol. Simul.* 31:79–93.

22. Murzin, A. G., A. M. Lesk, and C. Chothia. 1994. Principles determining the structure of β-sheet barrels in proteins. II. The observed structures. *J. Mol. Biol.* 236:1382–1400.

23. Murzin, A. G., A. M. Lesk, and C. Chothia. 1994. Principles determining the structure of β-sheet barrels in proteins. I. A theoretical analysis. *J. Mol. Biol.* 236:1369–1381.

24. Kale, L., R. Skeel, M. Bhandarkar, R. Brunner, A. Gursoy, N. Krawetz, J. Phillips, A. Shinozaki, K. Varadarajan, and K. Schulten. 1999. NAMD2: Greater scalability for parallel molecular dynamics. *J. Comput. Phys.* 151:283–312.

25. MacKerell, A. D., D. Bashford, M. Bellott, R. L. Dunbrack, J. D. Evanseck, M. J. Field, S. Fischer, J. Gao, H. Guo, S. Ha, D. Joseph-McCarthy, L. Kuchnir, K. Kuczera, F. T. K. Lau, C. Mattos, S. Michnick, T. Ngo, D. T. Nguyen, B. Prodhom, W. E. Reiher, B. Roux, M. Schlenkrich, J. C. Smith, R. Stote, J. Straub, M. Watanabe, J. Wiorkiewicz-Kuczera, D. Yin, and M. Karplus. 1998. All-atom empirical potential for molecular modeling and dynamics studies of proteins. *J. Phys. Chem. B.* 102:3586–3616.

26. Jorgensen, W. L., J. Chandrasekhar, J. D. Madura, R. W. Impey, and M. L. Klein. 1983. Comparison of simple potential functions for simulating liquid water. *J. Chem. Phys.* 79:926–935.

27. Essmann, U., L. Perera, M. L. Berkowitz, T. Darden, H. Lee, and L. G. Pedersen. 1995. A smooth particle mesh Ewald method. *J. Chem. Phys.* 103:8577–8593.

28. Ryckaert, J. P., G. Ciccotti, and H. J. C. Berendsen. 1977. Numerical integration of the cartesian equations of motion of a system with constraints: molecular dynamics of *n*-alkanes. *J. Comput. Phys.* 23: 327–341.

29. Feller, S. E., Y. Zhang, R. W. Pastor, and B. R. Brooks. 1995. Constant pressure molecular dynamics simulation: the Langevin piston method. *J. Chem. Phys.* 103:4613–4621.

30. Nina, M., D. Beglov, and B. Roux. 1997. Atomic radii for continuum electrostatics calculations based on molecular dynamics free energy simulations. *J. Phys. Chem. B.* 101:5239–5248.

31. Lide, D. R. 2004. CRC Handbook of Chemistry and Physics, 85th ed. CRC Press, Boca Raton, FL.

32. Paine, P. L., and P. Scherr. 1975. Drag coefficients for the movement of rigid spheres through liquid-filled cylindrical pores. *Biophys. J.* 15: 1087–1091.

33. Furini, S., F. Zerbetto, and S. Cavalcanti. 2006. Application of the Poisson-Nernst-Planck theory with space-dependent diffusion coefficients to KcsA. *Biophys. J.* 91:3162–3169.

34. Furini, S., F. Zerbetto, and S. Cavalcanti. 2007. Role of the intracellular cavity in potassium channel conductivity. *J. Phys. Chem. B.* 111: 13993–14000.

35. Mills, J. E. J., and P. M. Dean. 1996. Three-dimensional hydrogen-bond geometry and probability information from a crystal survey. *J. Comput. Aided Mol. Des.* 10:607–622.

36. Humphrey, W., A. Dalke, and K. Schulten. 1996. VMD: visual molecular dynamics. *J. Mol. Graph.* 14:33–38.

37. Walker, B., M. Krishnasastry, L. Zorn, and H. Bayley. 1992. Assembly of the oligomeric membrane pore formed by staphylococcal α-hemolysin examined by truncation mutagenesis. *J. Biol. Chem.* 267:21782–21786.

38. Jayasinghe, L., G. Miles, and H. Bayley. 2006. Role of the amino latch of staphylococcal α-hemolysin in pore formation: a co-operative interaction between the N terminus and position 217. *J. Biol. Chem.* 281:2195–2204.

39. Gu, L.-Q., M. Dalla Serra, J. B. Vincent, G. Vigh, S. Cheley, O. Braha, and H. Bayley. 2000. Reversal of charge selectivity in transmembrane protein pores by using noncovalent molecular adapters. *Proc. Natl. Acad. Sci. USA.* 97:3959–3964.

40. Nonner, W., D. P. Chen, and B. Eisenberg. 1999. Progress and prospects in permeation. *J. Gen. Physiol.* 113:773–782.

41. Coalson, R. D., and M. G. Kurnikova. 2005. Poisson-Nernst-Planck theory approach to the calculations of current through biological ion channels. *IEEE Trans. Nanobioscience.* 4:81–93.

42. O'Keeffe, J. T., I. Cozmuta, D. Bose, and V. Stolc. 2007. A predictive MD-Nernst-Planck model for transport in α-hemolysin: modeling anisotropic ion currents. *Chem. Phys.* 342:25–32.

43. Gu, L.-Q., S. Cheley, and H. Bayley. 2001. Prolonged residence time of a noncovalent molecular adapter, β-cyclodextrin, within the lumen of mutant α-hemolysin pores. *J. Gen. Physiol.* 118:481–494.

44. Smart, O. S., G. M. P. Coates, M. S. P. Sansom, G. M. Alder, and L. C. Bashford. 1998. Structure-based prediction of the conductance properties of ion channels. *Faraday Discuss.* 111:185–199.

45. Movileanu, L., S. Howorka, O. Braha, and H. Bayley. 2000. Detecting protein analytes that modulate transmembrane movement of a polymer chain within a single protein pore. *Nat. Biotechnol.* 18:1091–1095.

46. Howorka, S., L. Movileanu, X. Lu, M. Magnon, S. Cheley, O. Braha, and H. Bayley. 2000. A protein pore with a single polymer chain tethered within the lumen. *J. Am. Chem. Soc.* 122:2411–2416.

47. Sanchez-Quesada, J., M. R. Ghadiri, H. Bayley, and O. Braha. 2000. Cyclic peptides as molecular adapters for a pore-forming protein. *J. Am. Chem. Soc.* 122:11757–11766.